Electron spin-resonance study on Ce^{3+} in $BaLiF_3$

2000 J. Phys.: Condens. Matter 12 5917

(http://iopscience.iop.org/0953-8984/12/27/310)

J. Phys.: Condens. Matter **12** (2000) 5917–5928. Printed in the UK PII: S0953-8984(00)11473-0

Electron spin-resonance study on Ce^{3+} in $BaLiF_3$

M Yamaga†, M Honda‡, K Shimamura§, T Fukuda§ and T Yosida‖

† Department of Electrical and Electronic Engineering, Faculty of Engineering, Gifu University, Gifu 501-1193, Japan
‡ Faculty of Science, Naruto University of Education, Naruto 772-8502, Japan
§ Institute for Materials Research, Tohoku University, Sendai 980-8577, Japan
‖ Nakanihon Automotive College, Kamo 505-0077, Japan

Received 31 January 2000, in final form 30 May 2000

Abstract. Three distinct Ce^{3+} sites in $BaLiF_3$ crystals estimated from the optical spectra are associated with configurations of Ce^{3+} accompanied by different charge compensators. This assignment is consistent with the electron spin-resonance (ESR) result that there are two tetragonal Ce^{3+} centres distorted along the [001] axis and two orthorhombic Ce^{3+} centres distorted along the [110] axis in the absence of the cubic centre. The configurations of the Ce^{3+} centres correspond to the substitution for Ba^{2+} ions along the [001] and [110] axes with Li^+ ions and the Ba^{2+}-ion vacancies along the [001] and [110] axes. The dominant component of the Ce^{3+} luminescence spectrum with the peak at ∼320 nm and the large Stokes shift energy (∼8300 cm^{-1}) is assigned as due to the substitution for a Ba^{2+} ion along the [001] axis with a Li^+ ion. As the ionic radius (0.74 Å) of Li^+ is much smaller than that (1.60 Å) of Ba^{2+}, the Li substitution produces more space, resulting in the large lattice relaxation in the 5d excited state of Ce^{3+}.

1. Introduction

Recently, operations of optically pumped tunable solid-state lasers in the UV region using the 5d–4f transition of Ce^{3+} in the fluoride crystals $LiYF_4$ [1–3] and $LiCaAlF_6$ [4, 5] were reported. As energy levels of the 5d excited states of Ce^{3+} in crystals are strongly affected by the symmetry and strength of the Ce^{3+} crystal field, the optical transitions are assigned to a shift from the UV into the visible regions caused by varying the host crystals [6]. New Ce^{3+}-activated fluoride crystals capable of lasing with wider UV tunability, $SrAlF_5$ [7], $BaLiF_3$ (BLF) [8–10], BaF_2 [11], and $BaMgF_4$ [12], were grown and the spectroscopic features were reported.

In a previous paper [8], we reported three distinct luminescent centres of Ce^{3+} in the BLF crystal. Here we describe briefly the optical features of the three Ce^{3+} centres. As shown in figure 1, the intense luminescence spectrum with the peak at ∼320 nm excited at 240 nm, denoted by A, has a large Stokes shift (∼8300 cm^{-1}) [8–10]. The peak (∼340 nm) of the weak luminescence band excited at 280 nm, denoted by B, is shifted to lower energy. The very weak absorption band is observed at the low-energy tail of the 240 nm and 250 nm bands. One of the excitation bands detected by monitoring the intensity of the luminescence fixed at 380 nm has a peak at 280 nm. The peak of the lowest-energy absorption band corresponding to the B configuration is also shifted to lower energy than that for the A configuration. The Stokes shift energy (∼7800 cm^{-1}) is close to that for the A configuration. The weak luminescence band with the peak at 280 nm excited at 240 nm, denoted by C, has a Stokes shift energy of half that amount (∼4400 cm^{-1}), assuming that the excitation spectrum for the C configuration

0953-8984/00/275917+12$30.00

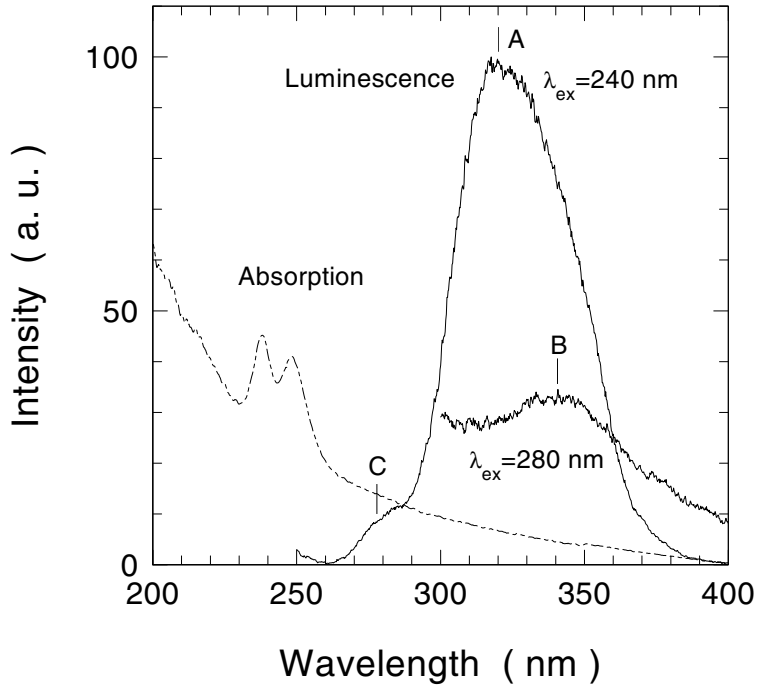

Figure 1. The absorption and luminescence spectra of Ce^{3+} in $BaLiF_3$ crystals [8]. The A and C components of the luminescence spectrum are observed with excitation at 240 nm, while the B component is observed with excitation at 280 nm.

is almost the same as for the A configuration. The lifetimes for the A and B configurations are 26 and 30 ns, respectively. The temperature (300 K) where the B-configuration lifetime starts to decrease is lower than that (400 K) for the A-configuration lifetime. As the increase in the lifetime corresponds to the decrease in the spin-allowed 5d–4f electric dipole transition probability, it is deduced that the 5d wavefunctions for the B configuration expand more outward than for the A configuration, or that the p-orbital states of the central Ce^{3+} and ligand F^- ions are mixed into the lowest 5d excited state through odd-parity distortions. The shift of the lowest 5d excited-state energy level to lower energy for the B configuration is expected to enhance the non-radiative decay rate associated with tunnelling between the excited- and ground-state potential wells. This is consistent with the temperature dependence of the lifetime.

As Ce^{3+} ions substitute for Ba^{2+} ions, the Ce^{3+} luminescent centres with A, B, and C configurations should be accompanied by different charge compensators. The aim of the present study is to identify the configurations of the Ce^{3+} centres in the BLF crystals using the electron spin-resonance (ESR) technique.

2. Experimental procedure

The BLF crystal has the cubic perovskite structure with space group O_h^1 shown in figure 2. The lattice constant is $a = 3.995$ Å. The anion-coordination polyhedron (cubo-octahedron) of Ba^{2+} with O_h symmetry is composed of twelve F^- ligand ions. A Ce^{3+} ion substitutes for a Ba^{2+} ion, which is accompanied nearby by a charge compensator.

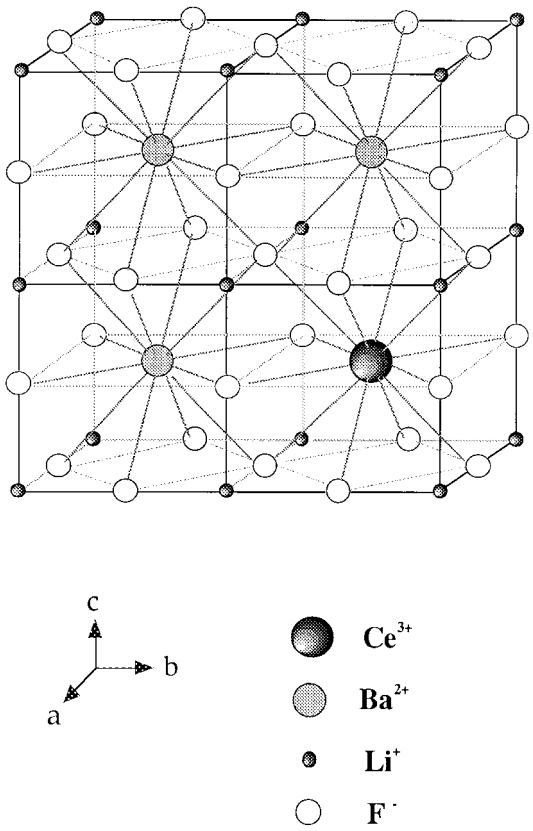

Figure 2. The perovskite crystal structure of $BaLiF_3$.

The details of the crystal growth were described in the previous paper [8]. The composition of the as-grown BLF crystal determined by the inductively coupled plasma (ICP) technique is represented by $Ce_{0.0002}$:$Ba_{0.987}Li_{0.992}F_{2.966}$. Laue x-ray diffraction was used to produce oriented samples, which were cut parallel to the crystallographic *a*-, *b*-, and *c*-axes with dimensions $2 \times 2 \times 2$ mm^3.

The ESR measurements were made in the temperature range of 4.2–300 K using a Bruker EMX10/12 X-band spectrometer with microwave frequencies of ∼9.685 GHz, a microwave power of 1 mW, and a 100 kHz field modulation. Angular variation of the ESR spectra was measured by rotating the sample in the cavity.

3. Experimental results

Figure 3 shows the ESR spectra of Ce^{3+} in the BLF crystal measured in the temperature range of 5–20 K with $\boldsymbol{B}$ parallel to the crystalline [001] axis. The spectrum observed at 5 K consists of several resonance lines denoted by T_1, R_1, and R_2. As temperature increases slightly up to 8 K, their signal intensities are drastically decreased, and new lines denoted by T_2 appear. The T_2 intensities have a maximum at ∼15 K and disappear above ∼25 K.

The ESR spectra were observed at 5 K and 13 K for magnetic field rotations in the (010) and $(1\bar{1}0)$ planes. Their angular variations of the g-values calculated using $h\nu = g\mu_B BS$,

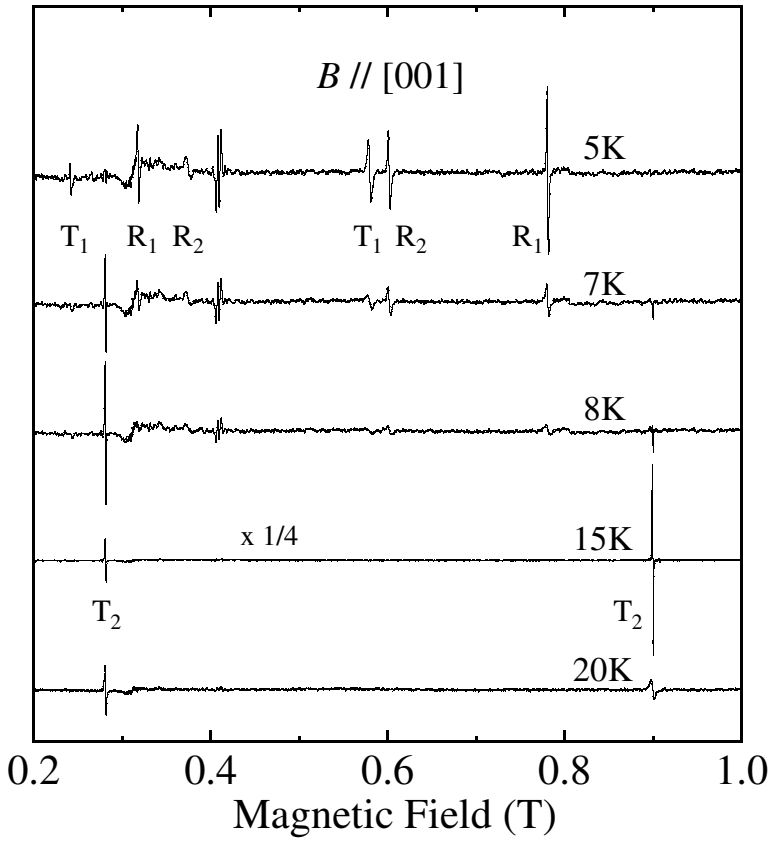

Figure 3. The temperature dependence of ESR spectra of Ce^{3+} in $BaLiF_3$ with $\boldsymbol{B} \parallel [001]$. Four distinct ESR signals are denoted by T_1, T_2, R_1, and R_2. The microwave frequencies are ~9.685 GHz, and the microwave power is 1 mW.

where μ_B is the Bohr magneton, B is the magnetic field, and $S = \frac{1}{2}$ is the effective spin for Ce^{3+} ions, are plotted in figures 4 and 5, respectively. The angular variation patterns of the (T_1, T_2) and (R_1, R_2) lines show tetragonal and orthorhombic symmetries, respectively. The orientation dependences of the g-values in figures 4 and 5 are analysed using an effective Hamiltonian appropriate to orthorhombic symmetry [13]:

$$\mathcal{H} = \mu_B g_x B_x S_x + \mu_B g_y B_y S_y + \mu_B g_z B_z S_z. \tag{1}$$

In the case of tetragonal symmetry, the relations $g_\parallel = g_z$ and $g_\perp = g_x = g_y$ are satisfied. The principal x-, y-, and z-axes for the tetragonal and orthorhombic symmetries, respectively, are the ([100], [010], [001]) and ([110], [$\bar{1}$10], [001]) axes of the crystal. The full curves in figures 4 and 5, calculated using equation (1) with the g-values for the T_1, T_2, R_1, and R_2 lines given in table 1, are in good agreement with the experimental points.

As shown in figure 3, the peak intensities of the resonance lines drastically decrease and become undetectable with increasing temperature. Such a temperature dependence is caused by the spin–lattice relaxation rate being enhanced at high temperatures [13, 14]. The direct, Raman, and Orbach processes lead to an increase of the homogeneous linewidth. The possibility of a direct process may be excluded since the observed broadening beyond detection is much too fast for this effect. The linewidth of the ESR spectrum with $\boldsymbol{B} \parallel [001]$, which is

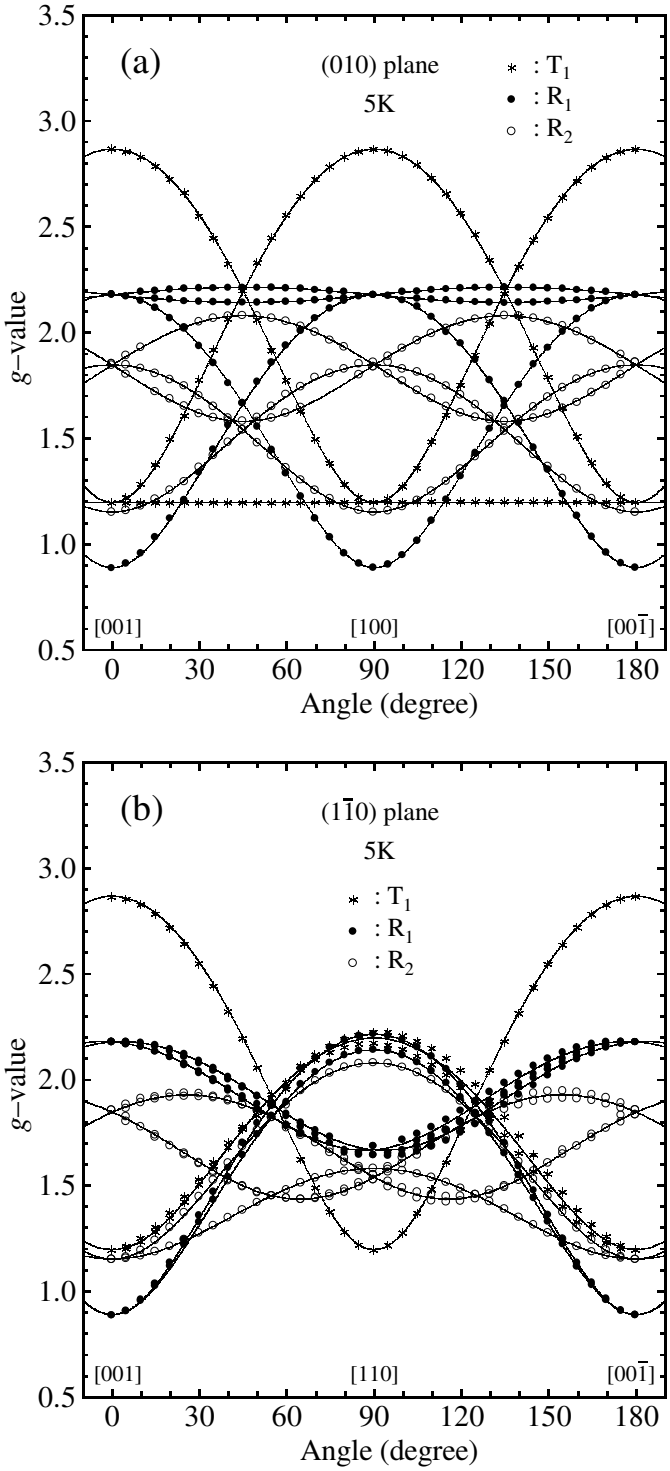

Figure 4. The angular dependence of the g-values of the ESR lines calculated using $h\nu = g\mu_B BS$ with $S = \frac{1}{2}$ for Ce^{3+} ions observed at 5 K in (a) the (010) plane and (b) the (1$\bar{1}$0) plane. The solid curves are calculated using equation (1) and the spin-Hamiltonian parameters in table 1.

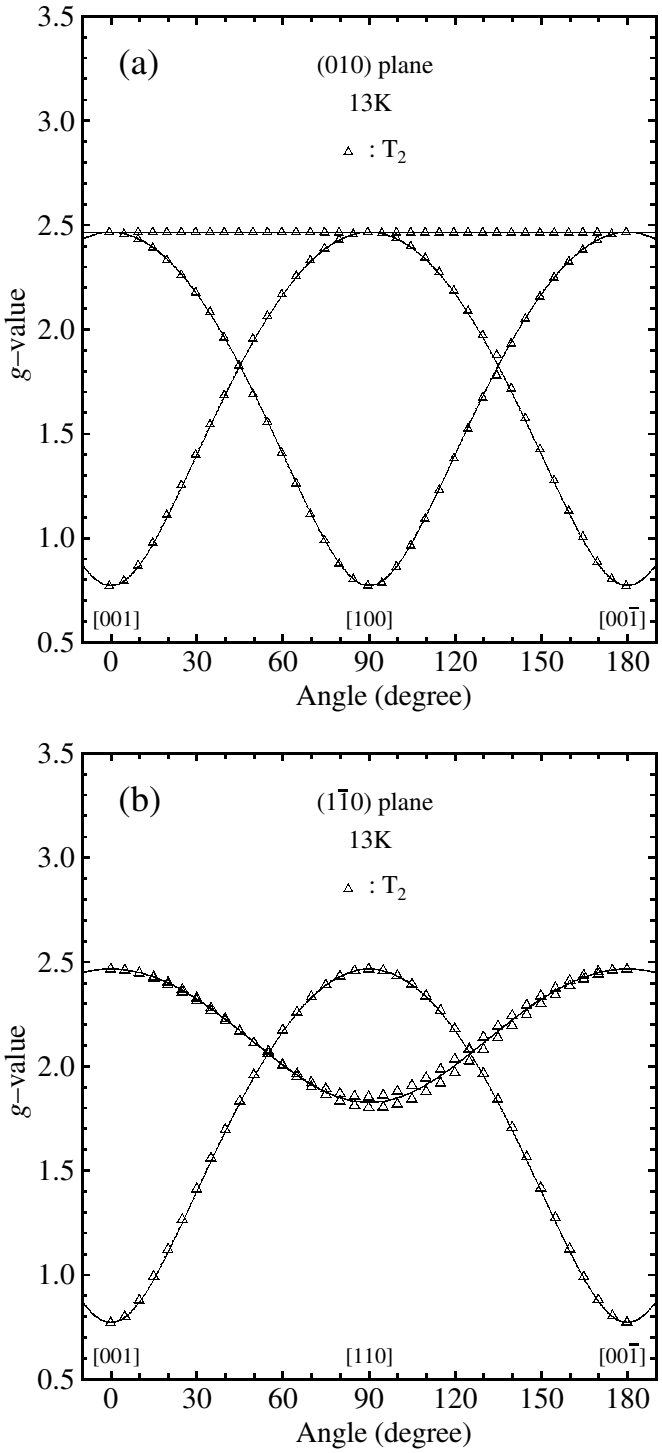

Figure 5. The angular dependence of the g-values of the ESR lines observed at 13 K in (a) the (010) plane and (b) the (1$\bar{1}$0) plane. The small splitting in (b) is due to misalignment (2°) between the crystalline axis and magnetic field direction. The solid curves are calculated using equation (1) and the spin-Hamiltonian parameters in table 1.

Table 1. The spin-Hamiltonian parameters in equation (1) and the activation energy in equation (2) for Ce^{3+} measured for the $BaLiF_3$ crystal.

Centre:	T_1	T_2	R_1	R_2
g-values	$g_\parallel = 2.866$	$g_\parallel = 0.772$	$g_z = 0.889$	$g_z = 1.152$
	$g_\perp = 1.196$	$g_\perp = 2.465$	$g_x = 2.214$	$g_x = 2.079$
			$g_y = 2.141$	$g_y = 1.580$
ΔE (cm^{-1})	30	134	38	40

equal to the peak-to-peak separation of the resonance, is plotted in figure 6 as a function of inverse temperature. The temperature dependence of the linewidth is calculated to be of the form [13]

$$\Gamma = a + bT^9 + c\exp(-\Delta E/kT). \tag{2}$$

The first term represents the temperature-independent inhomogeneous broadening. The second and third terms are associated with the Raman and Orbach processes with the thermal activation energy ΔE, respectively. The values of the fitting parameter ΔE for the T_1, T_2, R_1, and R_2 lines are summarized in table 1.

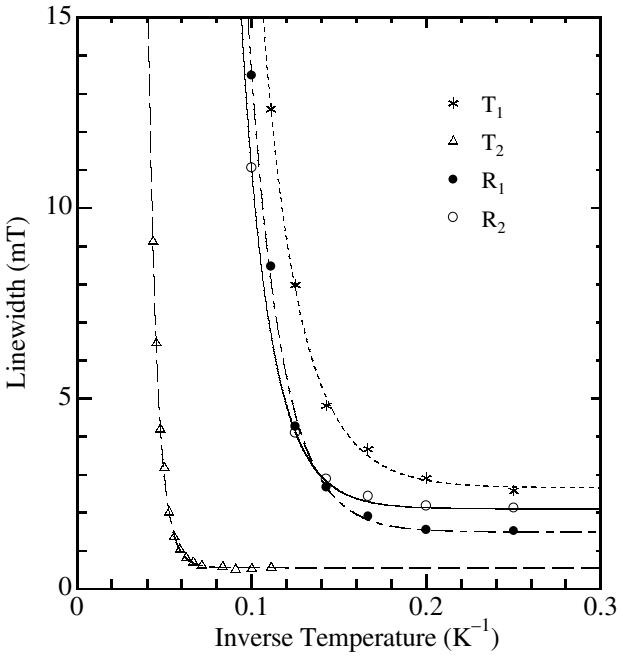

Figure 6. The temperature dependence of the linewidths for the T_1, T_2, R_1, and R_2 lines with $\boldsymbol{B} \parallel [001]$. The best-fitting curves are calculated using equation (2) and the activation energy ΔE in table 1.

4. Discussion

4.1. Assignment of the Ce^{3+} centres

A Ce^{3+} ion substitutes for a central Ba^{2+} ion in a cubo-octahedron in the BLF crystal in figure 2, which consists of twelve F^- ligands classified as two groups, one containing eight ligands in a cube and the other containing four ligands in an octahedron that lacks two ligands on the

crystalline [001] axis. As the valence of Ce^{3+} ions has an excess charge of +1 for Ba^{2+} ions, the charge compensators are required in the BLF crystal. The possible mechanisms of the charge compensation are as follows: (i) a Li^+ ion substitutes for a Ba^{2+} ion near to a Ce^{3+} ion, (ii) a vacancy is created at the nearest Li^+ site, and (iii) a single Ba^{2+} vacancy compensates for two Ce^{3+} ions. If a cubo-octahedron is accompanied by the charge compensator, the symmetry is reduced to lower symmetry from cubic. We discuss the g-tensors of the Ce^{3+} centres with tetragonal and orthorhombic symmetries, separately.

4.1.1. Tetragonal. The g-tensor of Ce^{3+} with tetragonal symmetry is discussed in terms of the wavefunctions of the ground state $^2F_{5/2}$. The Hamiltonian of the crystal field with a tetragonal distortion is

$$\mathcal{H}_{cry} = B_4(O_4^0 + 5O_4^4) + B_2^0 O_2^0 + B_4^0 O_4^0 \tag{3}$$

where the O_n^m are spin operators and B_4 and B_n^m are parameters of cubic and tetragonal fields, respectively [13]. In the case of strong tetragonal field ($|B_4| \ll |B_2^0|, |B_4^0|$), the eigenfunctions of the Hamiltonian are given by $|J, J_z\rangle = |\frac{5}{2}, \pm\frac{1}{2}\rangle, |\frac{5}{2}, \pm\frac{3}{2}\rangle$, and $|\frac{5}{2}, \pm\frac{5}{2}\rangle$ of $^2F_{5/2}$. As the spin operator O_4^4 in the cubic-field term mixes the spin states $|\frac{5}{2}, \mp\frac{3}{2}\rangle$ and $|\frac{5}{2}, \pm\frac{5}{2}\rangle$, the eigenfunctions of equation (3) are given by [13, 15]

$$\left|\pm\frac{\tilde{1}}{2}\right\rangle = \left|\frac{5}{2}, \pm\frac{1}{2}\right\rangle \tag{4}$$

$$\left|\pm\frac{\tilde{3}}{2}\right\rangle = \cos\theta\left|\frac{5}{2}, \pm\frac{5}{2}\right\rangle + \sin\theta\left|\frac{5}{2}, \mp\frac{3}{2}\right\rangle \tag{5}$$

$$\left|\begin{matrix}\alpha\\ \beta\end{matrix}\right\rangle = \sin\theta\left|\frac{5}{2}, \pm\frac{5}{2}\right\rangle - \cos\theta\left|\frac{5}{2}, \mp\frac{3}{2}\right\rangle. \tag{6}$$

The g-values for $|\pm\frac{\tilde{1}}{2}\rangle$ are

$$g_\parallel = \frac{6}{7} \qquad g_\perp = \frac{18}{7}. \tag{7}$$

The g-values for $|\pm\frac{\tilde{3}}{2}\rangle$ are calculated to be

$$g_\parallel = \frac{6}{7}|5\cos^2\theta - 3\sin^2\theta| \tag{8}$$

$$g_\perp = \frac{6}{7}|2\sqrt{5}\cos\theta\sin\theta|. \tag{9}$$

The g-values for $|\begin{smallmatrix}\alpha\\ \beta\end{smallmatrix}\rangle$ are calculated in the same way as for $|\pm\frac{\tilde{3}}{2}\rangle$.

The observed g-values ($g_\parallel = 0.772$, $g_\perp = 2.465$) for the T_2 lines are slightly smaller than those ($g_\parallel = 0.857$, $g_\perp = 2.57$) calculated for $|\pm\frac{\tilde{1}}{2}\rangle$. The small discrepancy can be explained by mixing $|\frac{7}{2}, \pm\frac{1}{2}\rangle$ and $|\frac{7}{2}, \mp\frac{7}{2}\rangle$ of the first excited state $^2F_{7/2}$ through the second-order perturbation [13, 15]. The modified eigenfunction is

$$\left|\pm\frac{\tilde{1}'}{2}\right\rangle = p_1\left|\frac{5}{2}, \pm\frac{1}{2}\right\rangle \pm q_1\left|\frac{7}{2}, \pm\frac{1}{2}\right\rangle \pm r_1\left|\frac{7}{2}, \mp\frac{7}{2}\right\rangle \tag{10}$$

where p_1, q_1, and r_1 are mixing parameters and $p_1^2 + q_1^2 + r_1^2 = 1$. The g-values are calculated to be

$$g_\parallel = \left|\frac{6}{7}p_1^2 + \frac{8}{7}(q_1^2 - 7r_1^2) + \frac{8\sqrt{3}}{7}p_1 q_1\right| \tag{11}$$

$$g_\perp = \left| \frac{18}{7} p_1^2 - \frac{32}{7} q_1^2 - \frac{4\sqrt{3}}{7} p_1 q_1 \right| \tag{12}$$

where the g-values with $p_1 = 1$ and $q_1 = r_1 = 0$ are equal to those in equation (7). The observed g-values for the T_2 lines are in good agreement with those ($g_\parallel = 0.772$, $g_\perp = 2.466$) calculated for $|\pm\tilde{\frac{1}{2}}'\rangle$ using equations (11) and (12) with $p_1 = 0.989$, $q_1 = 0.043$, and $r_1 = 0.134$. The small values of the mixing parameters q_1, r_1 satisfy the second-order perturbation requirements.

The observed g-values ($g_\parallel = 2.866$, $g_\perp = 1.196$) for the T_1 lines are reversed for the T_2 lines. This result suggests that the eigenfunction for the T_1 lines is close to $|\pm\tilde{\frac{3}{2}}\rangle$. The g-values ($g_\parallel = 3.06$, $g_\perp = 1.47$) calculated using equations (8) and (9) with $\theta = 25^\circ$ are slightly larger than the observed values. The difference in these g-values can also be explained in the same way as for the T_2 lines. The modified eigenfunction in equation (5) is

$$\left|\pm\tilde{\frac{3}{2}}'\right\rangle = p_2\left|\frac{5}{2}, \pm\frac{5}{2}\right\rangle + q_2\left|\frac{5}{2}, \mp\frac{3}{2}\right\rangle \pm r_2\left|\frac{7}{2}, \pm\frac{5}{2}\right\rangle \pm t_2\left|\frac{7}{2}, \mp\frac{3}{2}\right\rangle \tag{13}$$

where $p_2^2 + q_2^2 + r_2^2 + t_2^2 = 1$. The g-values are calculated to be

$$g_\parallel = \left| \frac{6}{7}(5p_2^2 - 3q_2^2) + \frac{8}{7}(5r_2^2 - 3t_2^2) + \frac{4}{7}(\sqrt{6}p_2 r_2 + \sqrt{10}q_2 t_2) \right| \tag{14}$$

$$g_\perp = \left| \frac{6}{7}(2\sqrt{5}p_2 q_2) - \frac{8}{7}(4\sqrt{3}r_2 t_2) - \frac{2}{7}(\sqrt{2}p_2 t_2 + \sqrt{30}q_2 r_2) \right| \tag{15}$$

where the g-values with $r_2 = t_2 = 0$ are equal to equations (8) and (9). In principle, it is difficult to determine the four parameters p_2, q_2, r_2, and t_2 from the two observed g-values and wavefunction normalization. Assuming that $p_2 \sim \cos 25^\circ$, $q_2 \sim \sin 25^\circ$ and $|r_2|, |t_2| \ll |p_2|, |q_2|$, the best fitting between the observed and calculated g-values was obtained by a least-squares regression technique. The g-values ($g_\parallel = 2.865$, $g_\perp = 1.196$) calculated for $|\pm\tilde{\frac{3}{2}}'\rangle$ using equations (14) and (15) with $p_2 = 0.873$, $q_2 = 0.378$, $r_2 = -0.281$, and $t_2 = -0.126$ fit the observed g-values quite well.

We consider the origin of the T_1 and T_2 lines with tetragonal symmetry, whose eigenfunctions are different from each other. The T_1 signals decrease rapidly with increasing temperature and disappear above 9 K. On the other hand, the T_2 signals appear above 6 K, have a maximum in intensity at 15 K, and disappear above 25 K. In addition, the $g_\parallel(T_2)$ line shape has only a negative component of the derivative line below 9 K and becomes symmetric above 10 K as shown in figure 3. An asymmetric line shape of the resonance is usually measured under conditions of adiabatic rapid passage, in which the sweep rate of the magnetic field is much faster than the spin–lattice relaxation rate [14]. As the spin–lattice relaxation rate is enhanced at high temperatures, the line shape changes from asymmetric to symmetric. If the spin state associated with the T_2 lines is assumed to be the first excited spin state in $^2F_{5/2}$, the T_2 lines are observed when the first excited spin levels are thermally populated. In this case, the spin–lattice relaxation rate between the first excited spin levels is expected to be comparable to or larger than that between the ground spin levels. This is inconsistent with the above observed results. Taking account of the result that the temperature-independent linewidth of the T_2 line in figure 6 is one fifth of that of the T_1 line, it is apparent that the T_1 and T_2 lines are due to different Ce^{3+} centres with different spin–lattice relaxation rates at low temperatures.

Next, we discuss the structure of the Ce^{3+} centres corresponding to the T_1 and T_2 lines with tetragonal symmetry. As the ground-state wavefunction for the T_2 centre is approximately $|\frac{5}{2}, \pm\frac{1}{2}\rangle$, the sign of B_2^0 is expected to be positive. In this case, the spin density expands toward

the [001] axis; that is, the Ce^{3+} cubo-octahedron may be elongated along the [001] axis. On the other hand, the wavefunction for the T_1 centre is approximately $|\frac{5}{2}, \pm\frac{5}{2}\rangle$, the sign of B_2^0 being negative. The cubo-octahedron may be compressed along the [001] axis. These tetragonal distortions along the [001] axis are strongly associated with Ba^{2+} sites along the [001] axis as shown in figure 2. There are two possible mechanisms of the charge compensation: one is the substitution for a Ba^{2+} ion of a Li^+ ion and the other is a Ba^{2+}-ion vacancy. As the former configuration produces effectively negative charge at the Ba site, the four F^- ions between the substitutional Li^+ ion and the Ce^{3+} ion are repulsed toward the Ce^{3+} ion and the Ce^{3+} ion moves toward the Li substitution. In consequence, the Ce^{3+} cubo-octahedron associated with the Li substitution is compressed along the [001] axis. In the latter case, the ions surrounding the vacancy should move in order to fill the space created by the vacancy. Rearrangement of the four F^- ions between the vacancy and the Ce^{3+} ion may cause elongation along the [001] axis. The larger distortion produces the larger splitting of $^2F_{5/2}$. As the value of ΔE in equation (2) is equal to the energy separation between the ground and first excited states of $^2F_{5/2}$, the distortion of the T_2 centre is expected to be much larger than that of the T_1 centre. In consequence, the T_1 and T_2 centres are associated with the substitution for Ba^{2+} of Li^+ and a Ba^{2+} vacancy along the [001] axis, respectively.

4.1.2. Orthorhombic. First, we discuss the g-values for the R_1 and R_2 lines assuming that these Ce^{3+} centres are approximated to be tetragonal. The approximate values of $g_\parallel = g_z$ and $g_\perp = \frac{1}{2}(g_x + g_y)$ for the R_1 and R_2 lines are set to $(g_\parallel, g_\perp) = (0.889, 2.178)$ and $(1.152, 1.830)$, respectively. These approximate g-values are in agreement with those, $(g_\parallel, g_\perp) = (0.890, 2.179)$ and $(1.152, 1.831)$, calculated using equations (11) and (12) with the parameters $(p_1, q_1, r_1) = (0.97, 0.16, 0.17)$ and $(0.96, 0.25, 0.15)$, respectively.

The difference in g_x and g_y for the R_1 and R_2 lines is induced by an orthorhombic distortion. The Hamiltonian of the crystal field including an orthorhombic distortion needs to have the spin operator $B_2^2 O_2^2$ added to equation (3). The eigenfunction is assumed to be

$$\left|\pm\frac{\tilde{1}}{2}''\right\rangle = p_3\left|\pm\frac{\tilde{1}}{2}'\right\rangle + q_3\left|\frac{5}{2}, \pm\frac{5}{2}\right\rangle + r_3\left|\frac{5}{2}, \mp\frac{3}{2}\right\rangle \tag{16}$$

where $p_3^2 + q_3^2 + r_3^2 = 1$. Assuming that the Zeeman terms connecting $\pm q_1|\frac{7}{2}, \pm\frac{1}{2}\rangle \pm r_1|\frac{7}{2}, \mp\frac{7}{2}\rangle$ in $|\pm\frac{\tilde{1}}{2}'\rangle$ and $q_3|\frac{5}{2}, \pm\frac{5}{2}\rangle + r_3|\frac{5}{2}, \mp\frac{3}{2}\rangle$ are neglected, the g-values obtained by McLaughlan and Forrester [16] are modified as follows:

$$g_x = \left|g_\perp p_3^2 + \frac{6}{7}(2\sqrt{5}q_3 r_3) + \frac{24\sqrt{2}}{7}p_3 r_3\right| \tag{17}$$

$$g_y = \left|g_\perp p_3^2 + \frac{6}{7}(2\sqrt{5}q_3 r_3) - \frac{24\sqrt{2}}{7}p_3 r_3\right| \tag{18}$$

$$g_z = \left|g_\parallel p_3^2 + \frac{6}{7}(5q_3^2 - 3r_3^2)\right|. \tag{19}$$

In the tetragonal case of $p_3 = 1$ or $p_3 = 0$, the g-values are equal to (equations (11), (12)) or (equations (8), (9)), respectively. The observed g-values for the R_1 and R_2 lines in table 1 are in good agreement with those, $(g_z, g_x, g_y) = (0.890, 2.216, 2.141)$ and $(1.152, 2.080, 1.581)$, calculated using equations (17), (18), and (19) and the parameters $(g_\parallel, g_\perp, p_2, q_2, r_2) = (0.889, 2.180, 0.998, -0.021, 0.007)$ and $(1.15, 1.83, 0.997, 0.062, 0.052)$, respectively. The small values of the mixing parameters q_3, r_3 satisfy the second-order perturbation requirements.

The R_1 and R_2 centres with orthorhombic symmetry, of which the principal axes are [110], [1$\bar{1}$0], and [001], are strongly associated with the charge compensators located along the [110] axis. As the larger difference in g_x and g_y gives the larger value of r_2, the orthorhombic distortion for the R_2 centre is expected to be much larger than that for the R_1 centre. These results lead us to deduce that the R_1 and R_2 centres correspond to the substitution for Ba^{2+} of Li^+ and a Ba^{2+} vacancy along the [110] axis, respectively.

There is the other possible charge-compensation mechanism where a vacancy is produced at a Li^+ ion along the [111] axis. However, no ESR signals with trigonal symmetry, corresponding to a [111] axis distortion, could be observed for the BLF crystal. The charge compensation favours the Ba^{2+} sites over the Li^+ sites.

4.2. Comparison with the optical results

The Ce^{3+} luminescence in the BLF crystal in figure 1 indicates that there exist A, B, and C configurations of Ce^{3+} in the crystal. The luminescence from the A configuration has a large Stokes shift ($\sim$8300 cm^{-1}). The peak energies of the lowest-energy absorption and luminescence bands from the B configuration are shifted to lower energy than those from the A configuration, and the Stokes shift energy ($\sim$7800 cm^{-1}) is close to that for the A configuration. The luminescence from the C configuration has a Stokes shift half that ($\sim$4400 cm^{-1}) of the A configuration.

The T_1 and R_1 centres obtained from the ESR spectra are associated with the Li substitution along the [001] and [110] axes, respectively. The substitution produces space in the nearest neighbour of the Ce^{3+} ion because the ionic radius (0.74 Å) of Li^+ is much smaller than that (1.60 Å) of Ba^{2+}. The distance between the Ce^{3+} and Ba^{2+} ions along the [110] axis is $\sqrt{2}$ times that along the [001] axis. Such a difference may appear in the electron–phonon coupling of Ce^{3+}—that is, the lattice relaxation of the 5d excited state of Ce^{3+}. The lattice relaxation for the T_1 centre is expected to occur more efficiently than that for the R_1 centre. Taking account of the fact that the Stokes shift energy is double the lattice relaxation energy, we see that the T_1 and R_1 centres correspond to the A and C configurations, respectively.

On the other hand, the T_2 and R_2 centres are assigned as due to Ce^{3+} accompanied by the vacancies of Ba^{2+} ions along the [001] and [110] axes, respectively. The vacancy produces a large deviation from the regular structure, resulting in a large energy shift of the 5d excited state. The peak of the lowest-energy absorption band for the B configuration is shifted to lower energy than that for the A configuration. This indicates that the B configuration is strongly associated with the T_2 and/or R_2 centres. However, they could not be distinguished optically.

5. Conclusions

The ESR results indicate that four Ce^{3+} centres are accompanied by different charge compensators. They are (i) the substitution for Ba^{2+} ions along the [001] and [110] axes of Li^+ ions and (ii) Ba^{2+}-ion vacancies along the [001] and [110] axes. These Ce^{3+} centres with tetragonal and orthorhombic symmetries correspond to three different (A, B, and C) configurations observed in the optical spectra. The proposed models for the Ce^{3+} centres can explain the energy levels, relaxation energy, and lifetime associated with the 5d excited states of Ce^{3+} obtained from the optical spectra.

Acknowledgments

This work was partially supported by the Research for the Future Programme 'Growth and characterization of single crystals for active elements' of the Japan Society for the Promotion of Science. One of authors (M Yamaga) is indebted to Corning for a Research Grant Award.

References

[1] Ehrlich T D J, Moulton P F and Osgood R M 1978 *Opt. Lett.* **4** 184
[2] Okada F, Togawa S and Ohta K 1994 *J. Appl. Phys.* **75** 49
[3] Yosida T, Yamaga M, Lee D, Han T P J, Gallagher H G and Henderson B 1997 *J. Phys.: Condens. Matter* **9** 3733
[4] Marshall C D, Speth J A, Payne S A, Krupke W F, Quarles G J, Castillo V and Chai B H T 1994 *J. Opt. Soc. Am.* B **11** 2054
[5] Yamaga M, Lee D, Henderson B, Han T P J, Gallagher H G and Yosida T 1998 *J. Phys.: Condens. Matter* **10** 3223
[6] Kodama N, Yamaga M and Henderson B 1998 *J. Appl. Phys.* **84** 5820
[7] Dubinskii M A and Schepler K L 1998 *J. Mod. Opt.* **45** 221
[8] Yamaga M, Imai T, Shimamura K, Fukuda T and Honda M 2000 *J. Phys.: Condens. Matter* **12** 3431
[9] Combes C M, Dorenbos P, van Eijk C W E, Gesland J Y and Ridnyi P A 1995 *J. Lumin.* **72–74** 753
[10] Marsman M, Andriessen J and van Eijk C W E 2000 *J. Lumin.* **87–89** 1023
[11] Wojtowicz A J, Szupryczynski P, Glodo J, Drozdowski W and Wisniewski D 2000 *J. Phys.: Condens. Matter* **12** 4097
[12] Yamaga M, Imai T and Kodama N 2000 *J. Lumin.* **87–89** 992
[13] Abragam A and Bleaney B 1970 *Electron Paramagnetic Resonance of Transition Ions* (Oxford: Clarendon)
[14] Weger M 1960 *Bell Syst. Technol. J.* **39** 1013
[15] Eliott R J and Stevens K W H 1952 *Proc. R. Soc* A **215** 437
[16] McLaughlan S D and Forrester P A 1966 *Phys. Rev.* **151** 311